Journal of Energy Storage 119 (2025) 116331

Contents lists available at ScienceDirect

Journal of Energy Storage

journal homepage: www.elsevier.com/locate/est

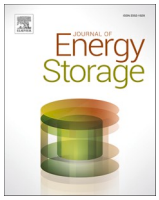

Research papers

Upside-down sodium ion capacitor: A non-presodiated system based on $Na_3V_2O_2(PO_4)_2F$ and biomass derived activated carbon

Jon Rodriguez-Romero [a], Nekane Nieto [a], Georghii Tchoudinov [b], Verónica Palomares [a], Luis Lezama [a], Seyed Javad Rezvani [b], Roberto Gunnella [b], Teófilo Rojo [a], Miguel Ángel Muñoz-Márquez [c,d], Idoia Ruiz de Larramendi [a,*], Eider Goikolea [a,*]

[a] Department of Organic and Inorganic Chemistry, Faculty of Science and Technology, University of the Basque Country UPV/EHU, Sarriena auzoa z/g. 48940 Leioa, Spain
[b] Physics Division, School of Science and Technology, University of Camerino, Via Madonna delle Carceri 9, 62032 Camerino, Italy
[c] Chemistry Division, School of Science and Technology, University of Camerino, Via Madonna delle Carceri-ChIP, 62032 Camerino, Italy
[d] National Reference Center for Electrochemical Energy Storage (GISEL)—INSTM, Via Giusti 9, 50121 Firenze, Italy

ARTICLE INFO

Keywords:
Na-ion capacitors
Hybrid energy storage systems
Sodium vanadium fluorophosphate
Activated carbon
Upside-down NICs
Rocking-chair

ABSTRACT

Hybrid systems between batteries and supercapacitors are designed to bridge the gap between both technologies, developing high-power, high-energy, and long cycle life energy storage devices. Moreover, in the urgent need to transition to a more sustainable energy model, sodium-based chemistries are an excellent alternative to lithium-based technologies. While various approaches have been tried in Na-ion capacitor (NIC) cell design, the upside-down NIC configuration remains underexplored. This consists of using a Na-containing battery-type cathode instead of an anode, which eliminates problems such as the need for pre-sodiation or Na-plating. This setup also allows the electrolyte concentration to stay stable, with ions exhibiting a rocking-chair motion, ensuring stable ionic conductivity during cycling. However, the potential window of these systems can be limited by the formation of the SEI on the capacitive negative electrode. Therefore, the aim of this paper is to explore the limitations of activated carbon (AC) in upside-down NICs through *ex-situ* X-ray photoemission spectroscopy (XPS) characterization and comprehensive monitoring of the electrode under various full-cell conditions, thereby assessing how far this configuration can be pushed in terms of energy. The proposed system features a high-rate capability cathode, a $Na_3V_2O_2(PO_4)_2F/C$ composite prepared via a novel one-step microwave synthesis, which delivers 64 mAh g^{-1} at 50C. The negative electrode employs a dried olive pits-derived AC with a surface area of 2138 m^2 g^{-1}. Together, they enable a full cell achieving up to 69 Wh kg^{-1} at 19 W kg^{-1} and 29 Wh kg^{-1} at 4915 W kg^{-1}, with an impressive capacity retention of 74 % after 10,000 charge-discharge cycles.

1. Introduction

Renewable energy sources are becoming increasingly crucial to address the problems of our current energy model based on fossil fuels. However, the intermittent nature of sustainable energies requires versatile energy storage systems (EESs) capable of offering a modular solution [1]. To try to overcome this, Li-ion batteries (LIBs) are the most used EESs, due to their massive ion-storage in the bulk material [2]. Nevertheless, this technology presents limitations such as a limited cyclability and a low power density, derived from the slow ion diffusion pathways and sluggish kinetics [3,4]. However, there is another energy storage technology, supercapacitors (SCs), which does operate with high power densities of up to 10 kW kg^{-1} and exhibit ultra-long cycle life [5]. These non-faradaic devices, however, deliver lower energy storage capacity values compared to those of LIBs, so, to bridge the gap between the two technologies, an ambitious type of device emerged, the so-called Li-ion capacitors (LICs) [6,7].

These devices aim to achieve both high energy and power densities by combining a faradaic electrode (LIB type) with one based on charge storage by adsorption/desorption (SC type). However, the huge and growing demand for lithium, combined with its low availability, makes the production of these devices unsustainable both economically and environmentally [8]. In this context, attempts to translate this approach to sodium-based energy storage have been reported since 2012, with the

* Corresponding authors.
E-mail addresses: idoia.ruizdelarramendi@ehu.eus (I. Ruiz de Larramendi), eider.goikolea@ehu.eus (E. Goikolea).

https://doi.org/10.1016/j.est.2025.116331
Received 11 December 2024; Received in revised form 15 February 2025; Accepted 17 March 2025
Available online 25 March 2025

publication of the first Na-ion capacitor (NIC) [9]. Indeed, sodium presents electrochemical properties analogous to those of lithium, thus making it possible to design electrochemically similar devices with the advantage of being a much more abundant and accessible material [10].

As in LICs, in conventional NICs the battery-type electrode is the negative electrode, while the positive electrode is capacitive one [11]. Upon charging, Na^+ ions are intercalated in the anode while PF_6^- ions are adsorbed on the surface of the positive electrode. This causes fluctuations in salt concentration during cycling, inevitably resulting in unstable ionic conductivity of the electrolyte [11–13]. In this configuration, the electrolyte concentration is also affected by the irreversible Na^+ intercalation and formation of the solid electrolyte interphase (SEI) on the anode also leads to a Na^+ consumption during cycles [14]. This intrinsic problem of NICs leads to the forced use of additives such as sacrificial salts, or the requirement of additional conditioning steps such as the pre-sodiation of the anode [9,15]. NICs and metal-ion hybrid capacitors in general also suffer from excessive polarization of the battery type anode and poor Na^+ diffusion at high charging/discharging rates [16]. However, significant efforts are being made in the research of anodes for NICs, particularly focusing on hard carbon (HC), transition metal oxides (TMOs), and 2D transition metal carbides and nitrides (MXenes). To further enhance their performance and facilitate intercalation at high rates, strategies such as doping, nanostructuring, and composite formation are employed. These approaches aim to create Na^+ diffusion pathways and improve the electrical and ionic conductivity of the materials.

However, another way to tackle some of the challenges faced by most NICs is through cell design. This can be achieved by using an inverted cell configuration, combining a battery-type cathode with a capacitive anode, known as the upside-down configuration. This electrode arrangement would allow only Na^+ to be used as the only charge carrier, which would be de-intercalated from the battery-type positive electrode and, simultaneously, adsorbed onto the surface of a capacitive negative electrode during discharge. This back-and-forth movement of electrolyte cations helps maintain a constant overall electrolyte concentration during cycling [17–20]. This mechanism, known as the “rocking-chair” mechanism, is characteristic of LIBs and other metal-ion batteries, such as sodium-ion batteries (NIBs) [17,21]. Furthermore, in this emerging upside-down configuration, preconditioning steps are not required during device fabrication, as SEI formation is unnecessary due to the absence of a battery-type anode. This enables a more straightforward manufacturing process while eliminating issues related to electrolyte concentration depletion. Moreover, removing the battery-type anode from consideration addresses the issue of Na-plating, which becomes particularly pronounced when attempting to drive carbonaceous anodes at high rates [22,23].

However, this relatively unexplored configuration still requires further research. We believe that the few existing reports on both LICs and NICs need to clarify the lights and shades of this approach. While it offers solutions to some challenges of the conventional configuration, as previously discussed, it may also be constrained by the operational potential window of the negative electrode. The formation of the SEI layer on the surface of the capacitive carbon at near-zero potentials when using a carbonate-based electrolyte is a concern that has been scarcely mentioned in previous reports. This electrically insulating layer could block the formation of the electrical double layer and obstruct access to micropores [24,25]. As a result, the total cell voltage, and consequently, its energy delivery, may be limited if the negative cut-off potential of the capacitive carbon is restricted to prevent SEI formation [10]. For this reason, it seems necessary to explore how far an upside-down NIC can be pushed in terms of potential window and energy output.

Similar to conventional hybrids, in upside-down hybrids, it is also necessary to strive for the best possible match in the rate capability between the cathode and anode, which operate at significantly different kinetics. This always proves to be challenging; fortunately, the growing research on cathodes for NIBs offers a wide variety of well-developed compounds that can be used in this approach, such as layered transition metal oxides, polyanionic compounds or Prussian blue analogues [26–32]. As Na^+ intercalation reactions exhibit slow kinetics, and since the capacitive electrode behaves much faster, the ion diffusion coefficient of the chosen cathode is a key factor when trying to balance the kinetics of both electrodes. Polyanionic compounds enable a fast diffusion of Na^+ through their 3D framework with a very low volumetric expansion, which makes them good candidates for this configuration. Their structure consists of metal oxide polyhedra and anion groups that share corners and/or edges, being Na^+ located in their interstitial sites and structural channels [33]. This also confers structural and thermal stability [34]. Among this family, $Na_3V_2O_2(PO_4)_2F$ (NVOPF) is highly valued for its theoretical capacity of ~130 mAh g^{-1} and high working voltages [35,36]. This material shows a pseudo-layered tetragonal structure with *I4/mmm* symmetry by connecting $[VO_5F]$ octahedrons and $[PO_4]$ tetrahedrons [37]. Two different Na^+ ion positions in the framework proffer the reversible de-intercalation of two Na^+ ions per formula unit, corresponding to the $V^{(V)}/V^{(IV)}$ redox pair. This leads to two voltage plateaus at 3.6 and 4.0 V vs. Na^+/Na [35,38,39]. However, as other phosphates, NVOPF is usually doped with heteroatoms [40–42] or coated with carbon [43–48] to deal with its low intrinsic electronic conductivity, which adds extra steps on the preparation. This could make the process more expensive and could hinder a potential scale-up, unless more effective mechanisms or less complicated syntheses are developed.

That is why we propose a facile, one-step, hydrothermal microwave synthesis for the preparation of the cathode material, which consists of as-synthesized NVOPF/C composite material mixed at the nanoscale. We report a full cell upside down NIC with that composite as the positive electrode, and a dried olive pit-derived AC as the negative electrode. Moreover, a three-electrode full cell electrochemical characterization and an SEI layer study were performed to clarify the effect of the SEI layer on AC negative electrodes, as well as to shed light on the limits of this less explored cell configuration.

2. Experimental section

2.1. Preparation of active materials

To prepare the AC, dried olive pits were pyrolyzed at 700 °C in a tubular furnace under N_2 flow. The resulting carbon was grounded using a mortar and mixed with KOH (activation agent) in a 1:6 mass ratio [49]. The activation was carried out in a tubular furnace at the same conditions (700 °C and a N_2 flow). The activated sample was thoroughly washed with 2 M HCl, distilled water, and then dried overnight at 80 °C. Carbon coated $Na_3V_2O_2(PO_4)_2F$ (NVOPF) was synthesized following a novel microwave assisted synthesis. $VO(C_5H_7O_2)$, H_3PO_4 and NaF were used as reagents in a molar ratio of 1.0:1.5:1.7, and 6 wt% of electrochemical grade carbon (Ketjen black) was also added to the solid mixture. $VO(C_5H_2O_2)$ was added to a mixture of 3 mL of ethanol and 1 mL of acetone followed by the addition of H_3PO_4, NaF and carbon black. The mixture was ultrasonicated for 10 min until it was completely homogeneous. After adding 20 mL of water, the prepared solution was exposed to 200 °C for 2 h using a microwave synthesizer (CEM MARS 5, 400 W).

2.2. Materials characterization

Powder X-ray diffraction (PXRD) patterns of the as-prepared composites were collected using a Panalytical X’Pert PRO equipped with a monochromatic Cu Kα radiation. The PXRD patterns of the ACs were also measured to check for crystalline impurities. Electron paramagnetic resonance (EPR) spectra were recorded on a Bruker ELEXSYS 500 spectrometer, operating at X band and equipped with a standard Oxford low-temperature device. The morphology of both samples was observed by scanning electron microscopy (SEM) using a JEOL JSM-7000F. The

specific surface area (SSA) value of AC was estimated applying the Brunauer-Emmett-Teller (BET) theory to the nitrogen adsorption/desorption isotherms measured at 77 K using a Quantachrome AutosorbIQ. Samples were previously degassed for 12 h at 200 °C and under 10^{-4} bar vacuum. Elemental CHN analyses were performed using a Euro EA Elemental Analyzer, EuroVector to determine by substraction the NVOPF content of the composite materials. Raman spectroscopy of the AC was performed in a Renishaw inVia spectrometer (514 nm Ar^{+} laser, 4 scans) 1000 and 2000 cm^{-1}. X-ray photoemission spectroscopy (XPS) measurements were performed via an in-house XPS apparatus based on a CLAM IV VG hemispherical spectrometer. The electrodes were transferred from the glovebox to the XPS load chamber using an Ar-filled glove bag, avoiding all contact with air. Base chamber pressure was 10^{-9} mbar. Measurements were carried out using a non-monochromatic focused Al Kα (hν = 1486.6 eV) radiation operated at 100 W, being the pass energy 50 eV for the wide scans and 20 eV for the regions.

2.3. Electrochemical characterization

Both AC and NVOPF/C electrodes were prepared starting from a slurry made of the active material, Super P C65 carbon black (Imerys) and poly(vynildifluoride) (PVDF) with a mass ratio of 8:1:1 in *N*-methyl pyrrolidone (NMP). The mixture was casted onto a battery grade Al foil. The casted slurry was then dried at 80 °C overnight and cut into circular electrodes of 12.7 mm in diameter. The mass loading of the electrodes was around 1–3 mg per electrode. All cells were assembled in an Ar-filled glove box (MBraun, O_2 and H_2O < 0.1 ppm) and stored in a 25 °C chamber during cycling. All the electrochemical performance tests were carried out using 1 M $NaPF_6$ in EC:PC (1:1 in *v*/v) (*E*-lyte) as electrolyte in three electrode Swagelock®-type cells in a VMP-3 (Bio-Logic) electrochemical workstation. Metallic sodium was used as the reference electrode, while glass microfiber discs (Whatman GF/A) were used as separators.

Before the electrochemical characterization of the full cell, NVOPF/C electrodes were tested in three-electrode cell configurations with Na counter and Na reference electrodes. Galvanostatic (GA) charge-discharge measurements were performed at C/10, C/5, C/2, C, 2C, 5C, 10C, 20C and 50C C-rates (C = 130 mA h g^{-1}). To avoid any overestimation of capacity, all capacity values are given per mass of composite material (NVOPF/C). AC electrodes were also tested in a three-electrode cell configuration using an oversized AC counter electrode and a Na reference at 0.1, 0.5, 1, 2, 5, 10, 15 and 20 A g^{-1} current densities (considering only the AC mass). This setup allowed testing the AC single electrode performance at high current rates, avoiding the kinetic mismatch of Na extraction/depletion and the fast performance of the AC that led into a capacity drop on previous half-cell tests. Cyclic voltammetries (CVs) were also performed in the case of AC electrodes at 5 mV s^{-1} to observe how the irreversible redox activity at low potentials affects the capacitance. The final NVOPF/C//AC full cell system was tested with 1:1 and 1:2 (NVOPF/C:AC) mass balances, performing GAs at C/5, C/2, C, 2C, 5C, 10C, 20C and 50C, which were calculated with the active material of the cathode. Finally, to investigate the long-term stability of the system, 10,000 GA cycles were carried out at 20C for selected mass balances.

3. Results and discussion

3.1. Physicochemical characterization of active materials

CHN analyses results suggest that the carbon content of the synthesized material is 15.9 %, while H and N are both 0.6 %. These values are an average between the different slots that are prepared in the microwave oven, which have presented a variance of <0.3 % in their composition. This minimal difference between samples has been treated as negligible throughout the entire investigation, since no differences have been observed in their electrochemical response or in their

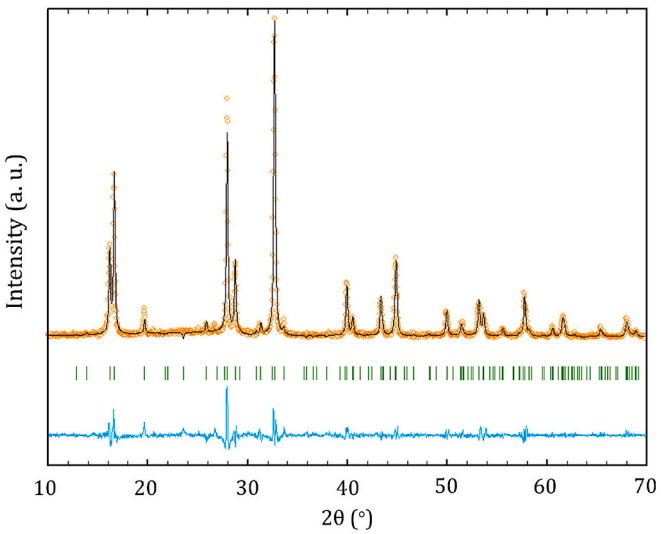

Fig. 1. Full Pattern matching of XRD diagram of NVOPF/C. Black line represents the fitting, red circles are experimental data, while the blue line at the bottom is the difference between them. (For interpretation of the references to colour in this figure legend, the reader is referred to the web version of this article.)

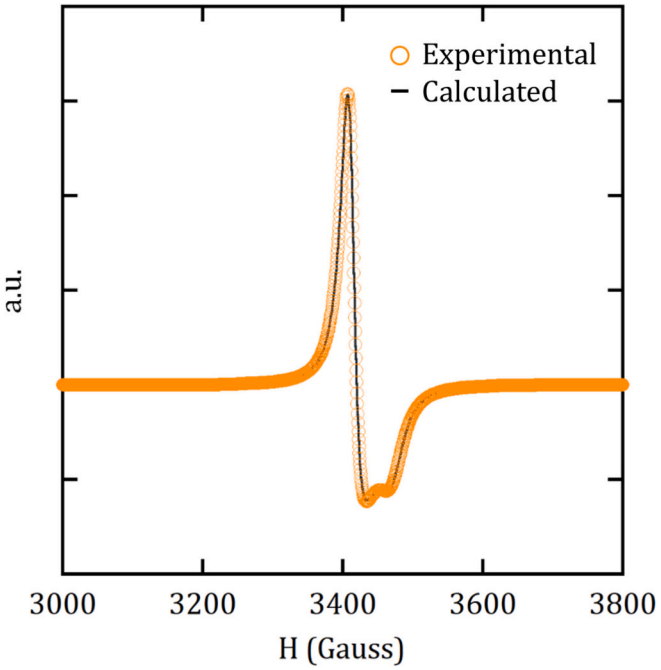

Fig. 2. EPR spectrum of NVOPF/C sample, experimental data are shown in orange and the fitting in black.

crystalline structure. It has been estimated that these percentages correspond to the subproduct from acetylacetonate decomposition and conductive carbon (Ketjen black) added in the synthesis to improve the conductivity of the material. As the XRD pattern of the material has not shown any impurity (see Fig. 1), it has been estimated that the remaining 84.1 % of the sample corresponds entirely to NVOPF. The experimental diffraction pattern of the synthesized material agrees well with $P4_2/mnm$ space group ((JCPDS 76–3845) [50], as shown in Fig. 1 [51–53].

The EPR spectrum of the raw NVOPF/C material is shown in Fig. 2. An axial signal centered at 3430 G is observed. A Lorentzian curve was used to fit the spectra ($g_{\parallel} = 1.9675$, $g^{\perp} = 1.9350$, $<g> = 1.9567$). These

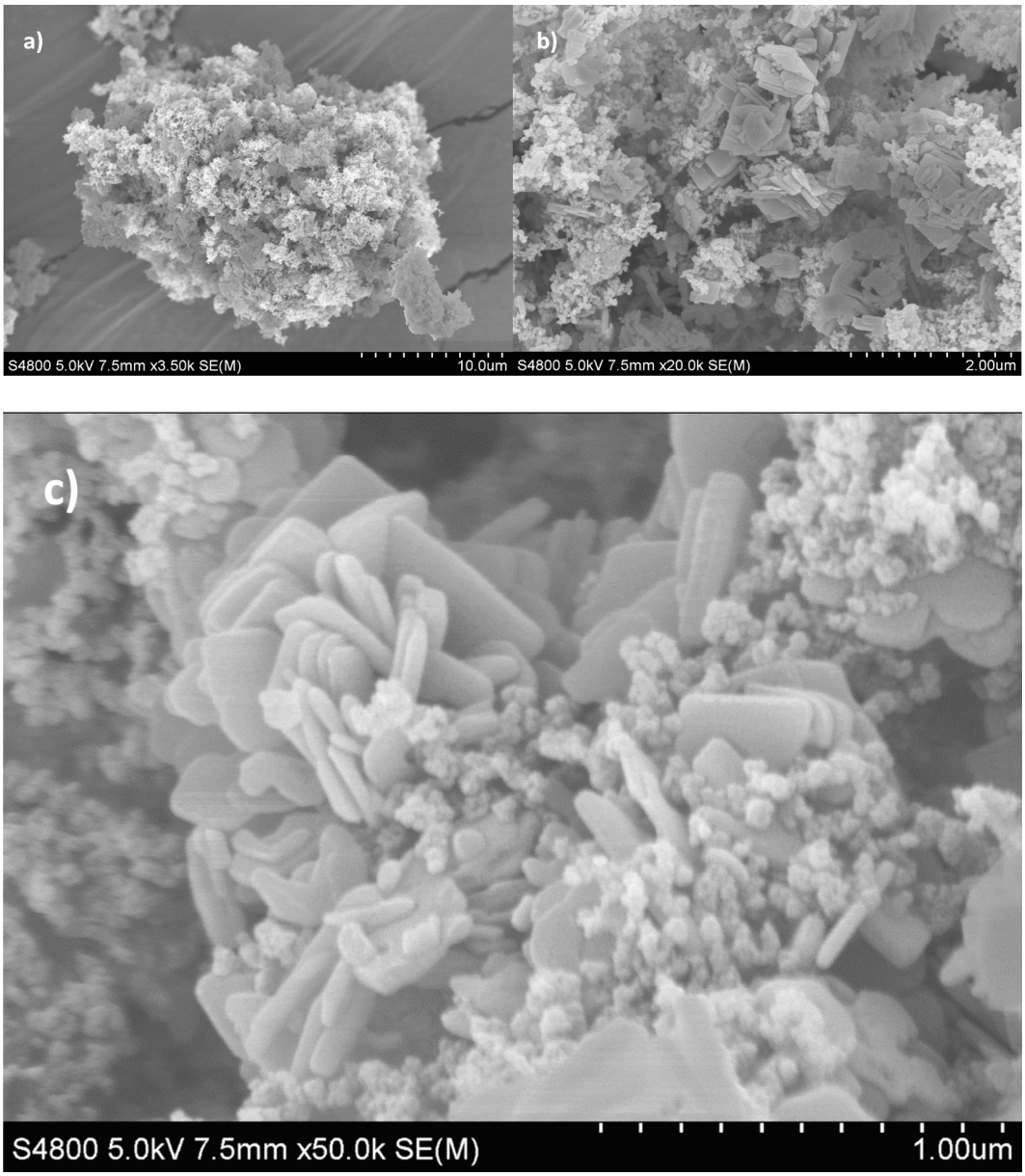

Fig. 3. SEM images of the NVOPF/C composite, cathode active material.

parameters confirm that the obtained material is $V^{(IV)}$ from the $Na_3(VO)_2(PO_4)_2F$ phase, since $2 > (g\| > g^{\perp})$ condition is fulfilled, typical of a VO^{2+} ion with an unpaired electron in a d_{xy} orbital. Also the narrow signal ($\Delta H_{pp} < 25$ G) indicates a high crystallization degree on the sample, and the absence of mixed valence phases [45]. This indicates that the obtained active material is purely $Na_3V_2O_2(PO_4)_2F$, with no presence of $V^{(III)}$. [54]

SEM images of the cathode material show that NVOPF particles and the carbon black form closely interlinked aggregates (Fig. 3 a, b). Inorganic particles mainly present platelet morphology, of about 250 nm length and a thickness lower than 100 nm, while conductive carbon particles range from 30 to 80 nm in size (Fig. 3 c) and are distributed around the NVOPF particles. This electron conductive network around NVOPF particles contributes to better electrochemical Na^+ extraction/insertion.

With respect to the AC, N_2 adsorption/desorption measurements revealed that the carbon was essentially microporous with a narrow size-distribution and a BET specific surface area of 2138 $m^2\ g^{-1}$ (Fig. 4a, b). Pore size distribution was calculated using a slit pore, 2D-NLDFT equilibrium model for N_2 at 77 K on carbon.

The XRD pattern recorded for the AC in Fig. 4 c shows two broad peaks at 20° and 43° of 2θ which correspond to (002) and (100) reflexions of carbon (JCPDF 75-16219), respectively. The presence of these peaks and the absence of planes (101) and (004) is a sign of low graphitization and high disorder [22,55]. This was also supported by the results obtained from Raman spectroscopy, in which the D (1340 cm^{-1}) and G (1580 cm^{-1}) bands of the carbon can be observed. The former reflects the stretching vibrations in the C—C bonds and the latter represents the defects in the structure [56]. The intensity ratio between this two bands ($I_D/I_G = 1.08$) indicates the presence of defects in the material [57–59]. The morphology observed in the SEM images of the AC shows the remains of the inherent microstructure of the plant precursor of the material, which now presents cracks and holes between 1 and 5 μm randomly distributed along the entire surface (Fig. S 1).

3.2. Electrochemical characterization of single electrodes

GA charge-discharge profiles of NVOPF/C show two plateaus at 3.6 V

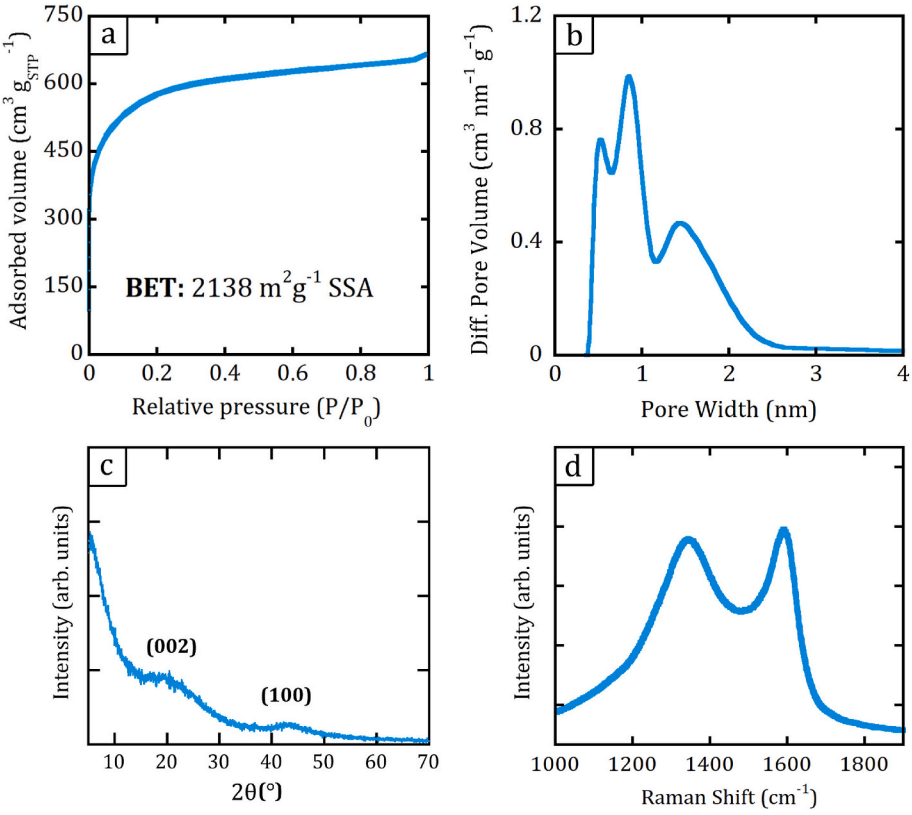

Fig. 4. a) N_2 Adsorption/desorption isotherm of the AC. b) Pore size distribution curve of the AC, calculated from the isotherm on the left. c) XRD pattern of the AC. d) Raman spectrum of the AC.

and 4.0 V (see Fig. 5). The composite material achieved capacities that ranged from 117 mAh g^{-1} at C/10 to 64 mAh g^{-1} at 50C. These results significantly surpass those previously obtained, both with and without carbon coating, representing an advancement not only in terms of performance but also in the simplicity of the synthesis method [45]. The composite was directly obtained through a one-step microwave synthesis, drastically reducing the synthesis time compared to other methods such as the hydrothermal approach. The obtained capacity values are comparable to those obtained with more costly and time-consuming synthesis methods, such as heteroatom doping, graphene coating or using nanostructured arrays [40–48]. This proves that the microwave-assisted method can provide an effective carbon-coating and enhance the capacity of the material by supplying a better electron conductive network.

To estimate the appropriate potential window for the negative AC electrode, as well as the occurrence of irreversible redox reactions and their impact on the electrochemical activity, CVs at 5 mV s^{-1} were performed. Thus, as can be seen in Fig. 6, when the AC is cycled between 1.6 and 3.0 V the CVs show the typical rectangular shape expected for capacitive materials (blue CV curve in Fig. 6). However, when extending the window to 0.2–3.0 V (purple CV curves in Fig. 6), a large irreversibility is observed from 1.5 V downwards. This redox activity could be related to the SEI formation, as shown by other carbonaceous materials [60,61]. The formation and stabilization of the SEI layer is accompanied by a progressive reduction of the capacitive behaviour of the AC, as suggested by the narrowing of the CV curve. Moreover, after cycling in the wider window, when the electrochemical behaviour of the composite material was tested back in the 1.6–3.0 V window (orange CV curve in Fig. 6), the capacitance obtained was found to be negligible. The primary composition of the SEI layer that is typically formed in carbonaceous electrodes in our electrolyte is based on NaF, Na_2CO_3 and organic matter such as EC and other C═O species [62]. This passivation layer acts as an ionic conductor and electrical insulator, thus helping the intercalation of ions in battery-type anodes [63]. However, as Fig. 6 shows, this SEI might be hindering the charge storage mechanism in capacitive electrodes. We believe this could be caused by access to the micropores of the AC being blocked, or by the insulating nature of the SEI blocking the electrical double layer formation [24,25]. Based on the observations from step 2 in Fig. 6, it can be inferred that, starting at 1.6 V, the formation of the SEI becomes more pronounced as the potential decreases, particularly when crossing the 0.9 V threshold, after which a more distinct redox bump can be observed. Therefore, the operational potential window of the negative AC electrode will be a limiting factor to be considered when designing the NIC full cell.

It is well known that the mass balance between the negative and the positive electrode is key for the optimum performance of the resulting full cell. In our case, knowing that the OCV of both electrodes is around 3.0 V, and that the cathode operates between 3.0 and 4.3 V, the capacity of the AC has been calculated from GA charge-discharge curves measured in the 1.6–3.0 V window (no redox activity). Fig. 7 shows that the negative AC electrode presents lower capacity than that of the NVOPF/C cathode, but the capability to perform at much higher current densities, as expected for a capacitive electrode [15].

Curves in Fig. 7 are not parallel, so to decide an appropriate mass balance it is necessary to estimate a target current for the full cell to work at. It was decided that the different currents at which the hybrid will be tested will be those corresponding to C-rates of the cathode, since it is the material most sensitive to high currents. As can be seen in Fig. 7, the cathode reaches higher capacities, and to calculate the mass balance, the capacities of both electrodes at 20C of the cathode have been compared. This c-rate has been considered as a sweet spot between current density and capacity, since it reaches 81 mAh g^{-1} at 2.6 A g^{-1}. Following the relationship of capacities at that current density, it has been established that the proper ideal mass balance should be 1:2 ($NVOPF_{fixed}$:AC). In addition, the AC discharge time for 2 A g^{-1} is almost half of that obtained for the cathode at 2.6 A g^{-1} (20C). This indicates

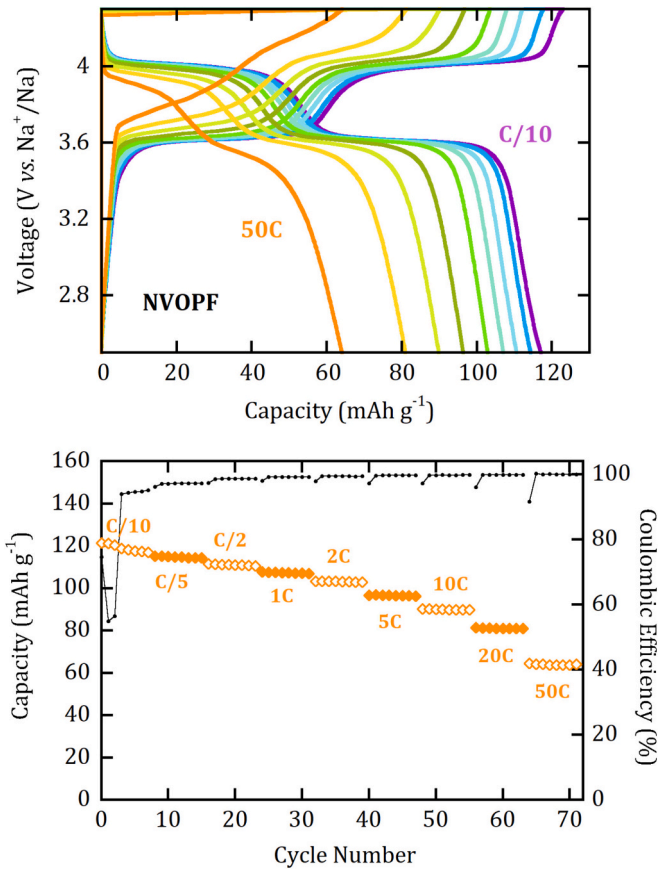

Fig. 5. GA curves for NVOPF/C in half cell configuration. 8th cycle is shown per different C rate (top). Capacity per cycle at C/10, C/5, C/2, 1C, 2C, 5C, 10C, 20C and 50C (bottom).

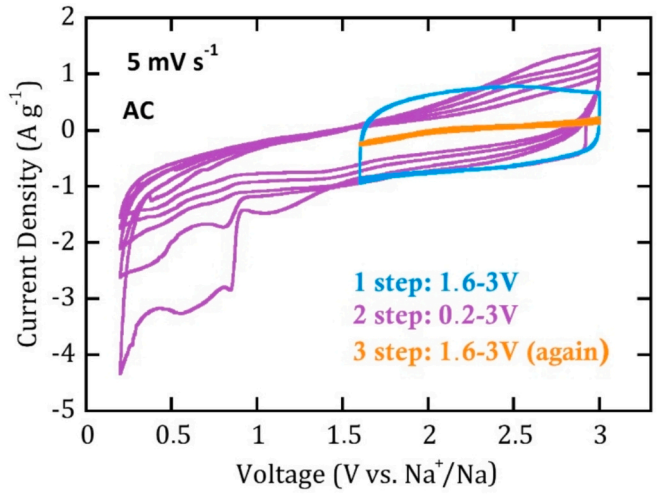

Fig. 6. CV between 3.0 and 1.6 V (blue). CVs between 3.0 and 0.2 V (purple). CV between 3.0 and 1.6 V, after the CV measurements in the 0.2–3.0 V window (orange). (For interpretation of the references to colour in this figure legend, the reader is referred to the web version of this article.)

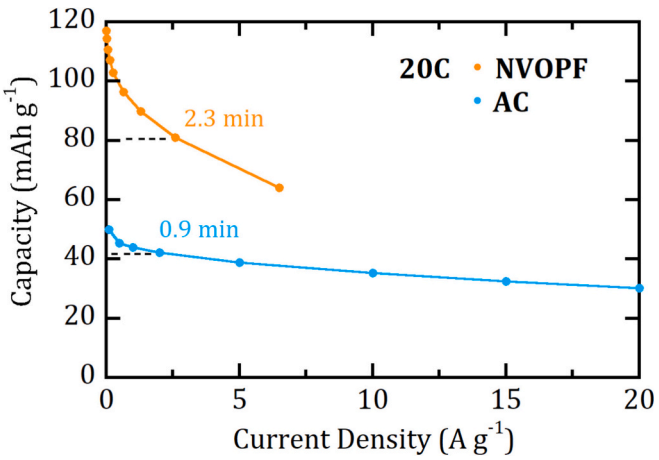

Fig. 7. Capacities of NVOPF/C and AC electrodes in half-cell configurations. Discharge times have been added to 20C of the cathode and 2 A g^{-1} of the AC.

that also in kinetic terms, the mass balance calculated using the charges, could be adequate.

3.3. *Electrochemical characterization of NVOPF/C//AC full cells*

To analyse the impact of the mass balance and cell voltage on the cell performance, three voltage windows (0–2.5 V, 0–3.0 V and 0–3.5 V) and two mass balances (1:1, and 1:2, NVOPF/C:AC) were studied. However, cells running at 0–3.5 V failed on the first cycles (C/5) so are only shown on Fig. S 2. We relate the capacity drop on those cells with the results obtained in the Fig. 6, in which we conclude that the SEI formation denies the charge adsorption on the AC. However, this will be later discussed and explored, backed by XPS results.

As Fig. 8 shows, the narrower window leads to very similar capacity values for both mass balances, getting about 17 mAh g^{-1} at 50C. When looking at the cells running in the 0–3 V cell voltage (Fig. 8, right), 1:1 system shows clearly larger capacity values than its counterpart at all current densities. At low current densities (or low C-rates) 0–3.0 V systems show higher capacity values than any of the 0–2.5 V systems; however, at high current densities (>5C) 1:2 (0–3.0 V) cell performs worse than any other does. It is noticeable that the capacity drop comparing from C/5 to 50C is more drastic in the 0–3.0 V window, with an average loss of 65 % of the initial capacity, rather than in the 0–2.5 V window, with a 49 % of capacity loss. This reflects that the cells operating at a wider cell voltage could be more sensitive to high currents. Even so, the cell running at 0–3.0 V with a 1:1 mass balance is the one that has performed the best at the selected current densities.

When calculating energy and power densities of the cells (see Fig. 9), the higher voltage and capacity of the cells working between 0 and 3 V translates on higher energy values when comparing to their counterparts. As expected, the symmetrical cell is the one showing the highest energy values: 69 Wh kg^{-1} at 19 W kg^{-1} and 29 Wh kg^{-1} at 4915 W kg^{-1}.

For a better understanding of the behaviour of each electrode, Fig. 10 provides a detailed breakdown of their voltage windows at 20C, for the four proposed cells. To fully grasp the conclusions derived from this figure, it is essential to refer to the observations made in Fig. 6. According to the results from the cyclic CV analysis, cut-off potentials for the negative electrode below 1.6 V could lead to the formation of the SEI, which may compromise the overall performance of the cell. Although the four full cells tested so far have not exhibited signs of capacity fade, Fig. 10 clearly shows that the negative electrodes in all cases have recorded potentials below 1.6 V. Given that SEI formation is likely more pronounced at lower potential values, particularly after crossing the 0.9 V threshold (Fig. 6), optimizing the system requires careful

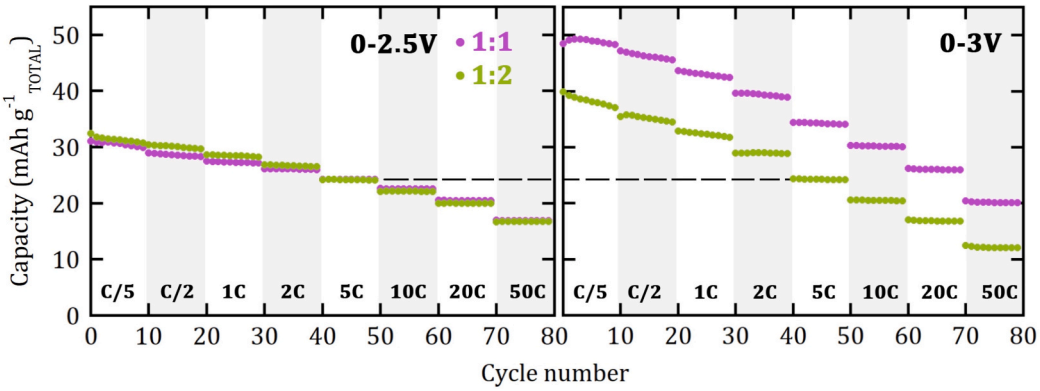

Fig. 8. Capacity of NVOPF/C//AC cells running at 0–2.5 V from C/5 to 50C (left). Capacity when running at 0–3.0 V (right). Capacity values are calculated considering the active masses of both electrodes. The currents used are those corresponding to the C-rates of the cathode.

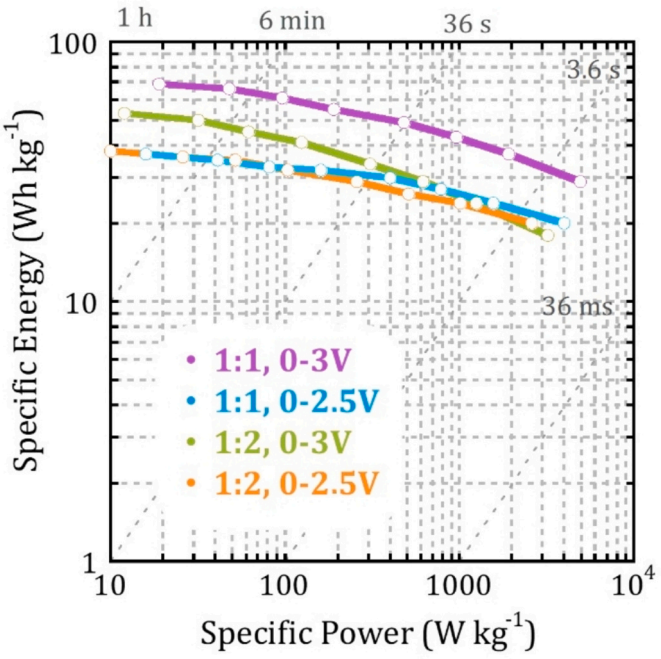

Fig. 9. Ragone plot, gravimetric values have been calculated with the total active mass of both electrodes.

consideration of the AC cut-off potential, as this parameter could significantly influence the long-term durability of the cell.

From Fig. 10 three major observations can be drawn. First, higher cell voltages (0–3 V) result in wider potential windows for both electrodes, along with lower cut-off potentials for the AC at each mass balance. Second, a lower relative amount of AC (mass balance 1:1) leads to an expansion of its potential window compared to that of the cathode, which, in the case of the cell operating at 0–2.5 V, does not even reach its second plateau. Third, conversely, in the 1:2 mass balance, both plateaus of the cathode are fully utilized, without registering cut-off potentials as negative as those observed in the other configurations.

As can be concluded from this three-electrode measurements, cells that exploit more the AC show the best performance. That raises the question of the risk involved in operating at those potentials. To shed some light on the SEI formation conditions, *ex-situ* XPS measurements of AC electrodes have been carried out. The objective behind this characterization is to observe how the composition of the surface of the electrode changes with cell voltage and how that can relate with its electrochemical performance.

3.4. XPS results of SEI layer on AC electrodes

The range of cut-off potentials for the AC negative electrodes in the tested full cells varies between 1.5 and 1 V (Fig. 10)., For this analysis, electrodes were prepared to represent three distinct stages of SEI formation, guided by their respective cut-off potentials. Additionally, the electrodes were extracted from full cells to ensure the results were as representative as possible of the actual system. The selected electrodes exhibited cut-off potentials of 1.6 V (cycled between 0 and 2.5 V), 1 V (cycled between 0 and 3.0 V), and 0.7 V (cycled between 0 and 3.5 V) (Fig. S 3), all obtained from cells with a 1:1 mass balance running at 10C. To gain further insight into the SEI at different states of charge, the AC electrodes were analyzed not only at their negative cut-off potentials during the first charge of the cells but also at their upper cut-off potential, after reaching 50 full cycles. This approach provides valuable information on the stability of the passivation layer under varying degrees of initial SEI formation. It is important to clarify that, even though cells running at 0–3.5 V have been previously discarded due to their failure at C/5 (Fig. S 2), this time, at 10C, there was no problem to perform 50 charge-discharge cycles. This could indicate that the high currents and fast kinetics when working at 10C do not favor the chemical reactions that led to the failure of the cells that ran at C/5.

Photoelectron peaks were measured from the C 1s, O 1s, Na 1s, F 1s and Cl 2p regions. Absolute binding energies were found at higher energies than those reported in the literature, so all spectra were calibrated to fit the C—C peak at 284.6 eV [64]. These shifts are due to the inability of the sample to compensate the charge accumulation coming from the electron removal during data acquisition. This charging effect of the surface is something expectable from samples like carbon electrodes that contain a given amount of insulating binder. Peak assignment was done following the data compilation made by M. A. Muñoz-Márquez et al. for hard carbon SEI components in Na ion batteries [65]. Voigt functions (70:30 Gaussian:Lorentzian) functions and *Shirley-type* backgrounds were used to fit the XPS spectra with *CasaXPS* software.

Fig. 11 shows the XPS spectra of the pristine and cycled electrodes. The pristine electrode, composed of AC and PVdF, contains mainly carbon and fluorine. The C1s spectrum of the pristine electrode shows an intense signal at 284.6 eV assigned to C—C sp^2 bonds, and other two contributions at 290.7 and 286.0 eV, corresponding with C—F_2 and C—H_2, respectively, from the PVdF. The presence of PVdF is further confirmed in the F1s spectrum by the presence of a signal at 689.1 eV, which corresponds to C—F_2. Moreover, a small signal is detected in the O1s spectrum, corresponding to the oxygenated species found in the surface of the AC, which could also contribute to the enlargement of the C—O peak located at 286.0 eV.

XPS results for the surface of electrodes charged one time (see Fig. 11) show how the peaks assigned to the **C**—C bond (284.6 eV, C—C, sp^2) and **C**—F_2 bond (290.7 eV, PVdF) on the C 1s region faint as the full

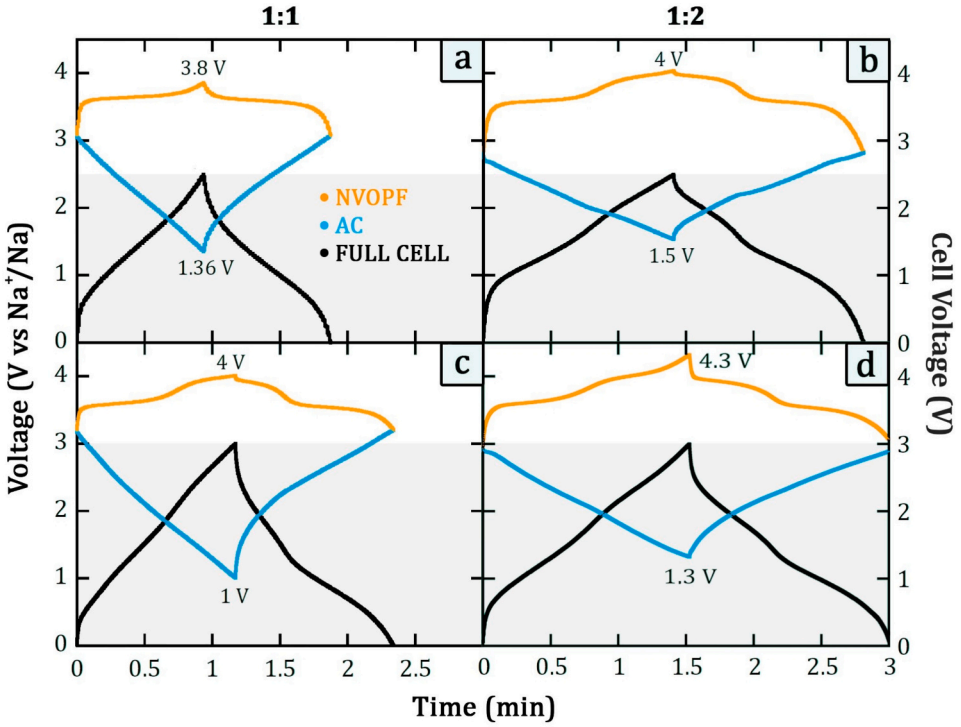

Fig. 10. GA charge-discharge profiles of the 8th cycle at 20C of the four different systems from Fig. 8. a) 1:1 at 0–2.5 V, b) 1:2 at 0–2.5 V, c) 1:1 at 0–3.0 V and d) 1:2 at 0–3.0 V.

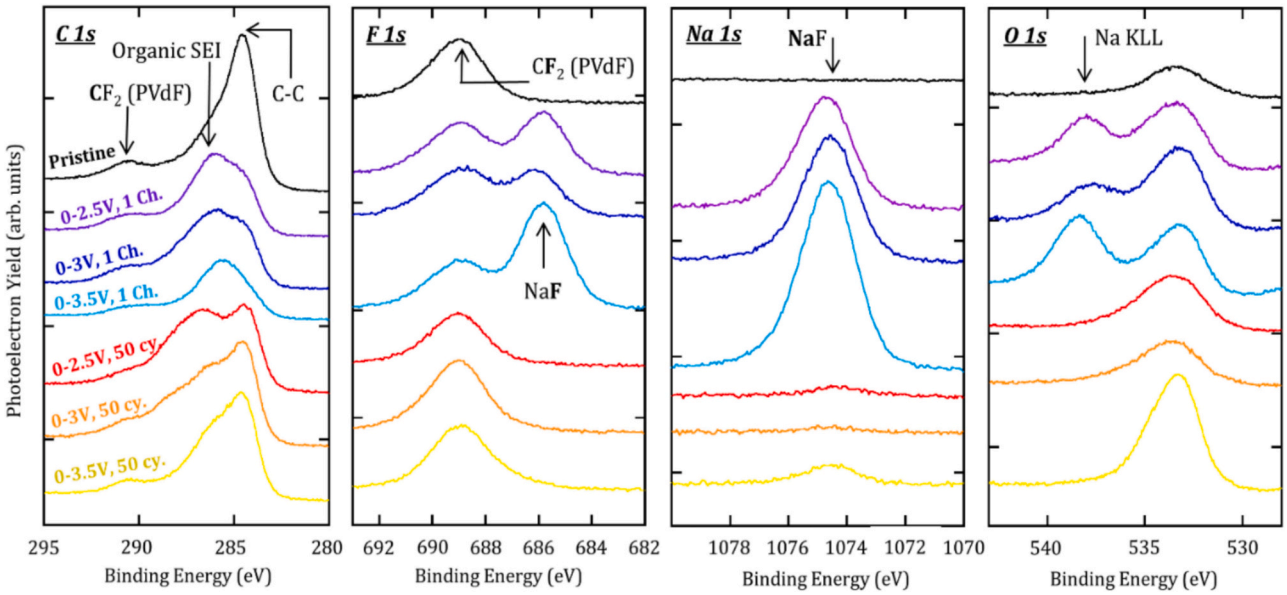

Fig. 11. XPS spectra corresponding to C 1s, O 1s, F 1s and Na 1s regions are shown for the pristine electrode and the cycled electrodes at different states of charge.

cell voltage increases. This could mean that the lower the potential of the AC in the charge, the thicker the passivation of the electrode. Regarding the signals that appear during the charge in the F 1s region, a new signal was registered at 686.4 eV, close to the 689.5 eV peak which is already present in the pristine electrode and is assigned to fluorine on PVdF. This new peak at 686.4 eV in the F 1s region is believed to come from the formation of NaF and, it is confirmed by the presence of Na in the charged samples as can be observed in the Na 1s region (1074.5 eV). The absence of $NaPF_6$ in the samples was confirmed since no photoelectron peaks were found in the P 2p region. In the O 1s region, the formation of a new peak at ~538 eV can be observed. This peak could be assigned to the organic part of the SEI layer, R-CH_2-**O**COONa. However, the Na signal from these compounds is not present, which is usually found at lower binding energies compared to NaF. Thus, the new peak at the O 1s line could belong to the $NaKL_1L_{23}$ Auger signal, which appears at 532 eV since its most intense peak, $NaKL_{23}L_{23}$ has been recorded in its proper position, around 493 eV (Fig. S 5) [66]. The presence of this Auger peak supports the appearance of Na on the surface, which is attributed to the formation of NaF. The key findings from the results described so far are that the C—C peak becomes less prominent, while the formation of NaF intensifies as the potential decreases. This clearly indicates the gradual passivation of the AC at lower potentials.

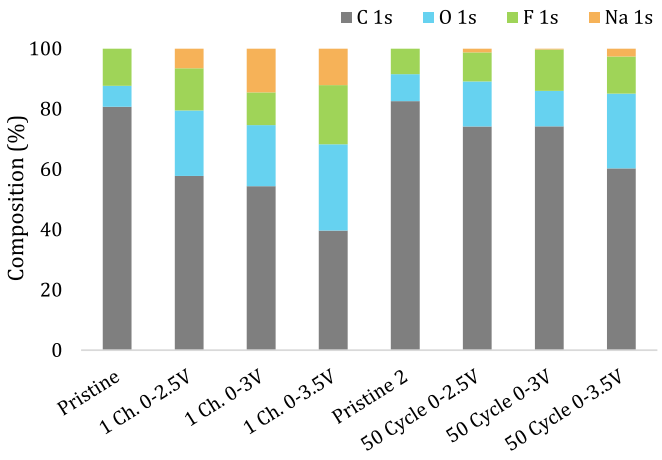

Fig. 12. Relative quantification of the surface composition (% at) of the pristine and cycled electrodes, as determined from the XPS data.

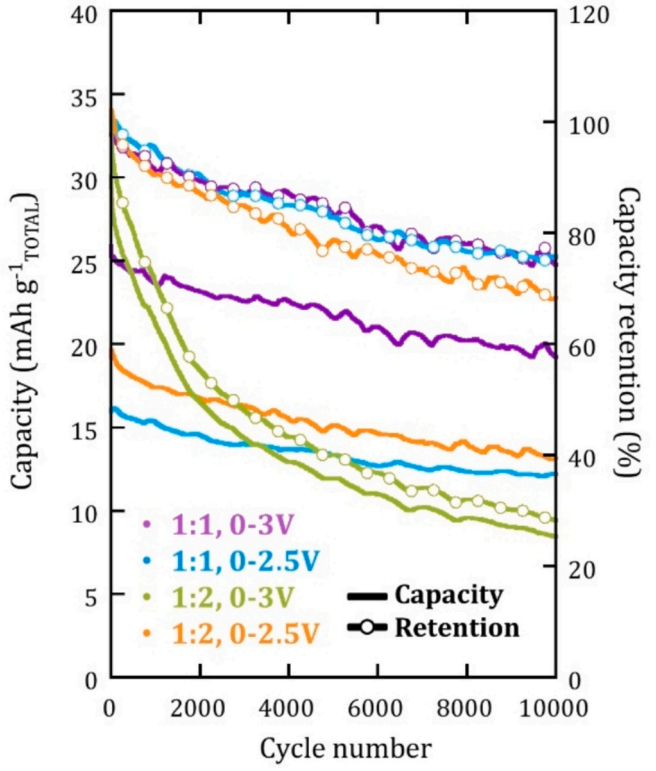

Fig. 13. Cycle capability measurements of the proposed systems at 20C. Capacity is calculated on the sum of active masses of both electrodes.

The three new peaks observed during the first charge (538 eV, 686.4 eV and 1074.5 eV) are not detectable in electrodes that have undergone 50 full cycles (and are therefore at their upper cut-off potential, around 3 V). This suggests that the passivation layer on the electrode may be re-dissolving each cycle. In the relative quantification of the XPS measurements (Fig. 12), it is evident that the amount of carbon detected on the surface decreases as the AC reaches more negative potentials, while the relative carbon content is restored in fully cycled electrodes. However, the electrode that fully cycled between 0 and 3.5 V does show a NaF residue, indicating that some of that passivation may be irreversible and, therefore, it could eventually passivate the electrode when cycling in wider potential windows.

3.5. Long term performance of NVOPF/C//AC full cells

Given that the passivation of the activated carbon is directly proportional to its cut-off potential during charging, as well as its degree of re-dissolution during cycling, it is necessary to conduct a cyclability study to assess how this might affect the system in the long term. To this end, cycling tests were performed at 20C over 10,000 charge-discharge cycles, following the four full-cell configurations previously proposed in the rate capability measurements.

As can be seen in Fig. 13, the initial capacity values of the cells working at 0–3 V are higher than those of the cells working at 0–2.5 V. However, among the 0–3.0 V cells, only the 1:1 cell achieved an acceptable capacity retention of 74 % after 10,000 cycles. The 1:2 cell showed higher capacities in the beginning but a capacity retention of only 28 %. In contrast, cells running between 0 V and 2.5 V did record an acceptable capacity retention when using both 1:1 (76 %) and 1:2 (68 %) mass balances. In this case, although both systems showed similar trends in the 1:2 cell capacity values were higher than in its counterpart.

Fig. 14 shows the variation of the electrode potentials (NVOPF/C positive electrode and AC negative electrode) over 10,000 charge-discharge cycles. The observed potential swings are like those obtained at 20C (see Fig. 10), as 1:2 0–3.0 V is the system with the highest cathode usage, and 1:1–0-3.0 V system shows the highest anode usage. The cells cycled between 0 and 2.5 V showed very similar behaviors. That is why it seems that at moderate cell voltages the mass balance does not seem to be such a critical factor, achieving acceptable capacity retentions at least in the first 10,000 cycles. However, when the cell voltage is pushed to higher values (0–3.0 V), the electrode performance depends deeply on the mass balance.

Within this imbalance, the most favourable results in terms of capacitance retention and specific capacitance have been for the 1:1 0–3.0 V system, which has shown a higher usage of the AC negative electrode over the positive NVOPF/C electrode. This suggests that a less use of the faradaic electrode favours the long-term performance of the proposed upside-down configuration. This conclusion is supported by the fact that battery electrodes generally have very limited cyclability compared to capacitive electrodes [11]. However, although a major use of the AC electrode has given the best results, a cut off potential that is too low for this electrode could hinder a capacitive mechanism based on ion adsorption, as we have seen previously in this report (Fig. 6). Since the cells that were measured between 0 and 3.5 V reached minimums of up to 0.7 V (Fig. S 3), but performed 50 cycles successfully, a final cyclability measurement was performed with a 1:1 electrode mass-balance and a 0–3.5 V window (Fig. S 4). This measurement was carried out to verify if the 0–3.5 V window is viable at high current densities although it was initially ruled out due to its collapse at C/5. However, the capacitance retention dropped 40 % after only 1200 cycles, and thereafter, it kept been fluctuating between 48 % and 31 %. In the profile (Fig. S 4, right), it can be seen how the cathode reaches potential values up to 4.75 V vs. Na^+/Na, which jeopardizes the integrity of the electrolyte [67]. Furthermore, even if the cell capacitance did not drop down to zero, the instability of the measurement supports discarding such large potential windows.

While leaving room for further optimization and study of the mechanisms of this hybrid, with what has been optimized to date we can say that cells with a 1:1 mass balance and cycled between 0 and 3 V have shown the most encouraging results in terms of energy density, power density and cycle life. The results obtained in this study are compared in Fig. 15 with the other upside-down hybrids found in the metal-ion capacitor (MIC) literature branch. Among this we find the following cathode//anode combinations: P2-NMC//ZDC [18], LVP-C//AC [68], NMNC-Al//CAC [20], LCPF//AC [69], $Na_{0.4}MnO_2$//AC [17], PBGO//AC [70] and NC-NVP//AC [71]. The last two are the ones that achieve the most similar results to those of our study, however they employ costly additives such as graphene oxide, or resort to processes such as doping the active materials, to deal with the handicaps of their active

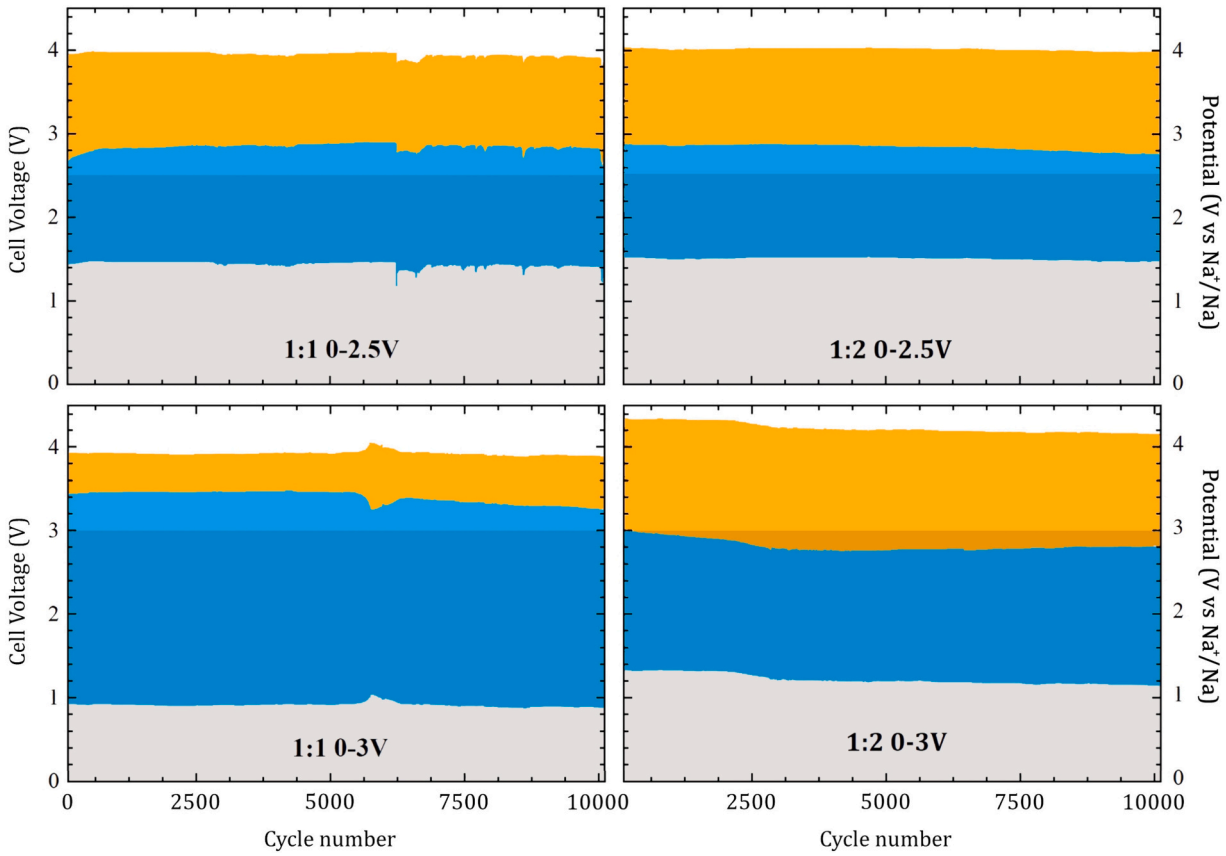

Fig. 14. Profiles of the potential windows of the positive and negative electrodes in four different systems.

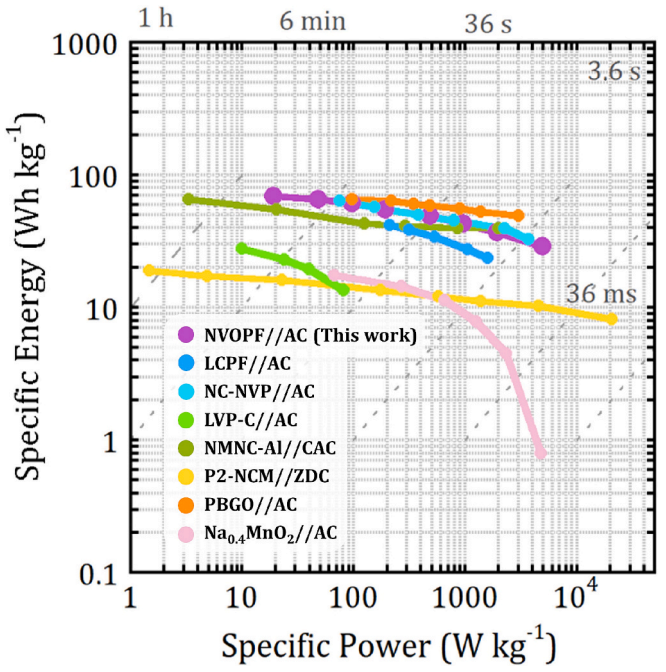

Fig. 15. Comparative Ragone-plot between this work and the state of the art in upside-down MICs.

materials. We believe that the simplicity of the synthesis proposed here as well as the use of a vegetable precursor such as olive pits give great value to this research in terms of sustainability and feasibility. In addition, because of the novelty of this area, we have found it necessary to further explore the behaviour of this type of hybrids, performing a detailed monitoring of each electrode and revealing the effects of the SEI layer on capacitive electrodes.

4. Conclusions

In this work we have developed upside-down Na-ion capacitors (NICs), exploring how this inverted configuration can solve some of the problems of the more common configurations where the capacitive electrode is placed at the positive side. Herein we take advantage of a high voltage and high capacity positive, $Na_3V_2O_2(PO_4)_2F/C$, and a biomass-derived activated carbon (AC). This approach gets rid of the problems of battery-type carbonaceous anodes commonly seen in NICs, such as a high first cycle irreversibility, the need of an electrode pre-conditioning and a poor Coulombic efficiency at high currents. The study has paid special attention to the monitoring of the two electrodes, observing how the different mass balances and cell voltages affect their performance. We have also focused on the effect of electrolyte decomposition on the surface of the AC electrode, analyzing the surface by XPS at various stages of the galvanostatic cycling. This has allowed us to optimize the system, helping us to understand the limitations of this NIC configuration.

With respect to the electrochemical performance, the system achieves up to 69 Wh kg^{-1} at 19 W kg^{-1} and 29 Wh kg^{-1} at 4915 W kg^{-1}, with an impressive capacity retention of 74 % after 10,000 charge-discharge cycles. This has been possible without the need to resort to more expensive and less sustainable solutions such as heteroatom doping, or additives such as graphene, carbon nanotubes and so on. Still, the work opens the door to improve this configuration by testing other carbons and other electrolyte compositions, which could help mitigating electrolyte degradation and, consequently, expanding the potential window of the cell and reaching even higher energies. This research

amplifies the portfolio of future storage solutions for the new scenario of energy trends.

CRediT authorship contribution statement

Jon Rodriguez-Romero: Writing – original draft, Visualization, Methodology, Investigation. **Nekane Nieto:** Writing – review & editing, Investigation. **Georghii Tchoudinov:** Investigation. **Verónica Palomares:** Writing – review & editing, Methodology. **Luis Lezama:** Resources, Investigation, Funding acquisition. **Seyed Javad Rezvani:** Resources, Methodology. **Roberto Gunnella:** Funding acquisition. **Teófilo Rojo:** Writing – review & editing, Funding acquisition, Conceptualization. **Miguel Ángel Muñoz-Márquez:** Writing – review & editing, Supervision, Resources. **Idoia Ruiz de Larramendi:** Writing – review & editing, Supervision, Project administration, Methodology, Funding acquisition. **Eider Goikolea:** Writing – review & editing, Supervision, Methodology, Funding acquisition, Conceptualization.

Declaration of competing interest

The authors declare that they have no known competing financial interests or personal relationships that could have appeared to influence the work reported in this paper.

Acknowledgements

This work was supported by Gobierno Vasco/Eusko Jaurlaritza (project IT1546-22); project PID2023-151153OB-I00 funded by MICIU/AEI/10.13039/501100011033 and by ERDF and the European Union; and project TED2021-131517B-C21 funded by MCIN/AEI/10.13039/501100011033 and by the European Union NextGenerationEU/PRTR.

Appendix A. Supplementary data

Supplementary data to this article can be found online at https://doi.org/10.1016/j.est.2025.116331.

Data availability

Data will be made available on request.

References

[1] C. Zhao, Q. Wang, Z. Yao, J. Wang, B. Sánchez-Lengeling, F. Ding, X. Qi, Y. Lu, X. Bai, B. Li, H. Li, A. Aspuru-Guzik, X. Huang, C. Delmas, M. Wagemaker, L. Chen, Y.-S. Hu, Rational design of layered oxide materials for sodium-ion batteries, Science 370 (6517) (2020) 708–711, https://doi.org/10.1126/science.aay9972.
[2] J.B. Goodenough, K.-S. Park, The Li-ion rechargeable battery: a perspective, J. Am. Chem. Soc. 135 (4) (2013) 1167–1176, https://doi.org/10.1021/ja3091438.
[3] M.R. Palacín, A. de Guibert, Why do batteries fail? Science 351 (6273) (2016) 1253292, https://doi.org/10.1126/science.1253292.
[4] M.D. Slater, D. Kim, E. Lee, C.S. Johnson, Sodium-Ion Batteries, Adv. Funct. Mater. 23 (8) (2013) 947–958, https://doi.org/10.1002/adfm.201200691.
[5] P. Simon, Y. Gogotsi, Perspectives for electrochemical capacitors and related devices, Nat. Mater. 19 (11) (2020) 1151–1163, https://doi.org/10.1038/s41563-020-0747-z.
[6] T. Morimoto, M. Tsushima, Y. Che, Performance of capacitors using organic electrolytes, MRS Online Proc. Libr. OPL 575 (1999) 357, https://doi.org/10.1557/PROC-575-357.
[7] G.G. Amatucci, F. Badway, A.D. Pasquier, T. Zheng, An asymmetric hybrid nonaqueous energy storage cell, J. Electrochem. Soc. 148 (8) (2001) A930, https://doi.org/10.1149/1.1383553.
[8] Z. Jian, B. Zhao, P. Liu, F. Li, M. Zheng, M. Chen, Y. Shi, H. Zhou, Fe2O3 nanocrystals anchored onto graphene nanosheets as the anode material for low-cost sodium-ion batteries, Chem. Commun. 50 (10) (2014) 1215–1217, https://doi.org/10.1039/C3CC47977C.
[9] K. Kuratani, M. Yao, H. Senoh, N. Takeichi, T. Sakai, T. Kiyobayashi, Na-ion capacitor using sodium pre-doped hard carbon and activated carbon, Electrochim. Acta 76 (2012) 320–325, https://doi.org/10.1016/j.electacta.2012.05.040.
[10] A.M. Glushenkov, A.V. Ellis, Cell configurations and electrode materials for nonaqueous sodium-ion capacitors: the current state of the field, Adv. Sustain. Syst. 2 (8–9) (2018) 1800006, https://doi.org/10.1002/adsu.201800006.
[11] F. Xing, Z. Bi, F. Su, F. Liu, Z. Wu, Unraveling the design principles of battery-supercapacitor hybrid devices: from fundamental mechanisms to microstructure engineering and challenging perspectives, Adv. Energy Mater. 12 (26) (2022) 2200594, https://doi.org/10.1002/aenm.202200594.
[12] V. Aravindan, J. Gnanaraj, Y.-S. Lee, S. Madhavi, Insertion-type electrodes for nonaqueous Li-ion capacitors, Chem. Rev. 114 (23) (2014) 11619–11635, https://doi.org/10.1021/cr5000915.
[13] S. Zhao, X. Sun, N. Wang, C. Li, Y. An, Y. Xu, K. Wang, X. Zhang, Y. Ma, Recent advances in hybrid Lithium-ion capacitors: materials and processes, ACS Appl. Energy Mater. 7 (24) (2024) 11553–11570, https://doi.org/10.1021/acsaem.4c00230.
[14] J. Liang, D. Wang, Design rationale and device configuration of lithium-ion capacitors, Adv. Energy Mater. 12 (25) (2022) 2200920, https://doi.org/10.1002/aenm.202200920.
[15] L. Xia, B. Tang, J. Wei, Z. Zhou, Recent advances in alkali metal-ion hybrid supercapacitors, Batter. Supercaps 4 (7) (2021) 1108–1121, https://doi.org/10.1002/batt.202000332.
[16] Z. Xu, F. Xie, J. Wang, H. Au, M. Tebyetekerwa, Z. Guo, S. Yang, Y.-S. Hu, M.-M. Titirici, All-cellulose-based quasi-solid-state sodium-ion hybrid capacitors enabled by structural hierarchy, Adv. Funct. Mater. 29 (39) (2019) 1903895, https://doi.org/10.1002/adfm.201903895.
[17] K. Wasiński, P. Półrolniczak, M. Walkowiak, Proof-of-concept study of a new type sodium-ion hybrid electrochemical capacitor with organic electrolyte, Electrochim. Acta 259 (2018) 850–854, https://doi.org/10.1016/j.electacta.2017.11.036.
[18] H. Gu, L. Kong, H. Cui, X. Zhou, Z. Xie, Z. Zhou, Fabricating high-performance sodium ion capacitors with P2-Na0. 67Co0. 5Mn0. 5O2 and MOF-derived carbon, J. Energy Chem. 28 (2019) 79–84.
[19] M.M. Sundaram, T. Watcharatharapong, S. Chakraborty, R. Ahuja, S. Duraisamy, P. T. Rao, N. Munichandraiah, Synthesis, and crystal and electronic structure of sodium metal phosphate for use as a hybrid capacitor in non-aqueous electrolyte, Dalton Trans. 44 (46) (2015) 20108–20120, https://doi.org/10.1039/C5DT03394B.
[20] K. Kaliyappan, Z. Chen, Atomic-scale manipulation of electrode surface to construct extremely stable high-performance sodium ion capacitor, Nano Energy 48 (2018) 107–116, https://doi.org/10.1016/j.nanoen.2018.03.021.
[21] S. Dong, N. Lv, Y. Wu, G. Zhu, X. Dong, Lithium-ion and sodium-ion hybrid capacitors: from insertion-type materials design to devices construction, Adv. Funct. Mater. 31 (21) (2021) 2100455, https://doi.org/10.1002/adfm.202100455.
[22] J. Ajuria, E. Redondo, M. Arnaiz, R. Mysyk, T. Rojo, E. Goikolea, Lithium and sodium ion capacitors with high energy and power densities based on carbons from recycled olive pits, J. Power Sources 359 (2017) 17–26, https://doi.org/10.1016/j.jpowsour.2017.04.107.
[23] M.D. Casal, N. Díez, S. Payá, M. Sevilla, Cork-derived carbon sheets for high-performance Na-ion capacitors, ACS Appl. Energy Mater. 6 (15) (2023) 8120–8131, https://doi.org/10.1021/acsaem.3c01212.
[24] W. Gu, G. Yushin, Review of nanostructured carbon materials for electrochemical capacitor applications: advantages and limitations of activated carbon, carbide-derived carbon, zeolite-templated carbon, carbon aerogels, carbon nanotubes, onion-like carbon, and graphene, WIREs Energ. Environ. 3 (5) (2014) 424–473, https://doi.org/10.1002/wene.102.
[25] V. Khomenko, E. Raymundo-Piñero, F. Béguin, High-energy density graphite/AC capacitor in organic electrolyte, J. Power Sources 177 (2) (2008) 643–651, https://doi.org/10.1016/j.jpowsour.2007.11.101.
[26] L. Zhao, J. Ni, H. Wang, L. Gao, Na0.44MnO2–CNT electrodes for non-aqueous sodium batteries, RSC Adv. 3 (18) (2013) 6650–6655, https://doi.org/10.1039/C3RA23032E.
[27] X. Ma, H. Chen, G. Ceder, Electrochemical properties of monoclinic NaMnO2, J. Electrochem. Soc. 158 (2011) A1307, https://doi.org/10.1149/2.035112jes.
[28] C.-Y. Yu, J.-S. Park, H.-G. Jung, K.-Y. Chung, D. Aurbach, Y.-K. Sun, S.-T. Myung, NaCrO2 cathode for high-rate sodium-ion batteries, Energy Environ. Sci. 8 (7) (2015) 2019–2026, https://doi.org/10.1039/C5EE00695C.
[29] Q. Wang, J. Xu, W. Zhang, M. Mao, Z. Wei, L. Wang, C. Cui, Y. Zhu, J. Ma, Research progress on vanadium-based cathode materials for sodium ion batteries, J. Mater. Chem. A 6 (19) (2018) 8815–8838, https://doi.org/10.1039/C8TA01627E.
[30] B.-K. Zou, Y. Shao, Z.-Y. Qiang, J.-Y. Liao, Z.-F. Tang, C.-H. Chen, LiMPO4 and derived NaMPO4 (M = Mn, Fe, Mg) with excellent electrochemical properties for lithium/sodium ion batteries, J. Power Sources 336 (2016) 231–239, https://doi.org/10.1016/j.jpowsour.2016.10.075.
[31] W. Li, F. Zhang, X. Xiang, X. Zhang, Nickel-substituted copper Hexacyanoferrate as a superior cathode for aqueous sodium-ion batteries, ChemElectroChem 5 (2018) 350–354, https://doi.org/10.1002/celc.201700958.
[32] P. Ge, S. Li, H. Shuai, W. Xu, Y. Tian, L. Yang, G. Zou, H. Hou, X. Ji, Ultrafast sodium full batteries derived from X-Fe (X = Co, Ni, Mn) Prussian blue analogs, Adv. Mater. 31 (3) (2019) 1806092, https://doi.org/10.1002/adma.201806092.
[33] X. Li, S. Jiang, S. Li, J. Yao, Y. Zhao, T. Bashir, S. Zhou, S. Yang, W. Li, W. Zhu, T. Liu, J. Zhao, L. Gao, Overcoming the rate-determining kinetics of the $Na_3V_2O_2(PO_4)_2F$ cathode for ultrafast sodium storage by heterostructured dual-carbon decoration, J. Mater. Chem. A 9 (19) (2021) 11827–11838, https://doi.org/10.1039/D1TA02250D.
[34] T. Liu, L. Gao, J. Chen, Q. Chen, H. Lei, L. Wang, X. Kong, Revealing the structural reversibility of high-performance surface-enhanced NVOPF cathode materials for sodium ion batteries, J. Phys. Chem. C 124 (50) (2020) 27378–27386, https://doi.org/10.1021/acs.jpcc.0c08654.
[35] M. Xu, P. Xiao, S. Stauffer, J. Song, G. Henkelman, J.B. Goodenough, Theoretical and experimental study of vanadium-based fluorophosphate cathodes for

rechargeable batteries, Chem. Mater. 26 (10) (2014) 3089–3097, https://doi.org/10.1021/cm500106w.
[36] J. Xu, J. Chen, L. Tao, Z. Tian, S. Zhou, N. Zhao, C.-P. Wong, Investigation of Na3V2(PO4)2O2F as a sodium ion battery cathode material: influences of morphology and voltage window, Nano Energy 60 (2019) 510–519, https://doi.org/10.1016/j.nanoen.2019.03.063.
[37] X. Wang, C. Niu, J. Meng, P. Hu, X. Xu, X. Wei, L. Zhou, K. Zhao, W. Luo, M. Yan, L. Mai, Novel K $_3$ V $_2$ (PO $_4$) $_3$ /C bundled nanowires as superior sodium-ion battery electrode with ultrahigh cycling stability, Adv. Energy Mater. 5 (17) (2015) 1500716, https://doi.org/10.1002/aenm.201500716.
[38] Y. Yin, F. Xiong, C. Pei, Y. Xu, Q. An, S. Tan, Z. Zhuang, J. Sheng, Q. Li, L. Mai, Robust three-dimensional graphene skeleton encapsulated Na3V2O2(PO4)2F nanoparticles as a high-rate and long-life cathode of sodium-ion batteries, Nano Energy 41 (2017) 452–459, https://doi.org/10.1016/j.nanoen.2017.09.056.
[39] P. Serras Malillos, High Voltage Cathodes for Na-Ion Batteries: Na3V2O2x(PO4)2F3-2x System, 2014 (doi:10/13077).
[40] P. Du, K. Mi, F. Hu, X. Jiang, X. Zheng, Mn–doped hollow Na3V2O2(PO4)2F as a high performance cathode material for sodium ion batteries, Eur. J. Inorg. Chem. 2021 (13) (2021) 1256–1262, https://doi.org/10.1002/ejic.202001159.
[41] M. Peng, D. Zhang, L. Zheng, X. Wang, Y. Lin, D. Xia, Y. Sun, G. Guo, Hierarchical Ru-doped sodium vanadium fluorophosphates hollow microspheres as a cathode of enhanced superior rate capability and ultralong stability for sodium-ion batteries, Nano Energy 31 (2017) 64–73, https://doi.org/10.1016/j.nanoen.2016.11.023.
[42] Nguyen, L. H. B.; Olchowka, J.; Belin, S.; Camacho, P. S.; Duttine, M.; Iadecola, A.; Fauth, F.; Carlier, D.; Masquelier, C.; Croguennec, L. Monitoring the Crystal Structure and the Electrochemical Properties of Na3(VO)2(PO4)2F through Fe3+ Substitution.
[43] X. Shen, J. Zhao, Y. Li, X. Sun, C. Yang, H. Liu, Y.-S. Hu, Controlled synthesis of Na3(VOPO4)2F cathodes with an ultralong cycling performance, ACS Appl. Energy Mater. 2 (10) (2019) 7474–7482, https://doi.org/10.1021/acsaem.9b01458.
[44] H. Jin, J. Dong, E. Uchaker, Q. Zhang, X. Zhou, S. Hou, J. Li, G. Cao, Three dimensional architecture of carbon wrapped multilayer Na3V2O2(PO4)2F Nanocubes embedded in graphene for improved sodium ion batteries, J. Mater. Chem. A 3 (34) (2015) 17563–17568, https://doi.org/10.1039/C5TA03164H.
[45] P. Serras, V. Palomares, P. Kubiak, L. Lezama, T. Rojo, Enhanced electrochemical performance of Vanadyl(IV)Na3(VO)2(PO4)2F by ex-situ carbon coating, Electrochem. Commun. 34 (2013) 344–347.
[46] G. Deng, D. Chao, Y. Guo, Z. Chen, H. Wang, S.V. Savilov, J. Lin, Z.X. Shen, Graphene quantum dots-shielded Na3(VO)2(PO4)2F@C nanocuboids as robust cathode for Na-ion battery, Energy Storage Mater. 5 (2016) 198–204, https://doi.org/10.1016/j.ensm.2016.07.007.
[47] M. Xu, L. Wang, X. Zhao, J. Song, H. Xie, Y. Lu, J.B. Goodenough, Na3V2O2(PO4)2F/graphene sandwich structure for high-performance cathode of a sodium-ion battery, Phys. Chem. Chem. Phys. 15 (31) (2013) 13032–13037, https://doi.org/10.1039/C3CP52408F.
[48] Y. Mao, J.A. Alonso, M.T. Fernández-Díaz, C. Sun, Nitrogen-doped carbon coated Na3V2O2(PO4)2F as a cathode for high-performance sodium-ion batteries, J. Electroanal. Chem. 975 (2024) 118763, https://doi.org/10.1016/j.jelechem.2024.118763.
[49] E. Redondo, J. Carretero-González, E. Goikolea, J. Ségalini, R. Mysyk, Effect of pore texture on performance of activated carbon supercapacitor electrodes derived from olive pits, Electrochim. Acta 160 (2015) 178–184, https://doi.org/10.1016/j.electacta.2015.02.006.
[50] C.-H. (Matt) Lai, D.S. Ashby, N.H. Bashian, J. Schoiber, T.-C. Liu, G.S. Lee, S.-Y. Chen, P.-W. Wu, B.C. Melot, B.S. Dunn, Designing the charge storage properties of Li-exchanged sodium vanadium fluorophosphate for powering implantable biomedical devices, Adv. Energy Mater. 9 (18) (2019) 1900226, https://doi.org/10.1002/aenm.201900226.
[51] T. Roisnel, J. Rodriguez-Carvajal, WinPLOTR: a windows tool for powder diffraction pattern, Analysis 378 (2001) 118–123, https://doi.org/10.4028/www.scientific.net/MSF.378-381.118.
[52] A.A. Tsirlin, R. Nath, A.M. Abakumov, Y. Furukawa, D.C. Johnston, M. Hemmida, H.-A. Krug von Nidda, A. Loidl, C. Geibel, H. Rosner, Phase separation and frustrated square lattice magnetism of {Na1.5VO(PO)4}F0.5, Phys. Rev. B 84 (1) (2011) 014429, https://doi.org/10.1103/PhysRevB.84.014429.
[53] Y.-M. Yin, C. Pei, W. Xia, X. Luo, D.-S. Li, Recent advances and perspectives on the promising high-voltage cathode material of Na3(VO)2(PO4)2F, Small 19 (44) (2023) 2303666, https://doi.org/10.1002/smll.202303666.
[54] P. Serras Malillos, High Voltage Cathodes for Na-Ion Batteries Na3V2O2x(PO4)2F3-2x System, Ph.D. Thesis,, UPV-EHU, UPV-EHU, Leioa, Spain, 2014.
[55] R. Raavi, S. Archana, P. Adinarayana Reddy, P. Elumalai, Performances of dual carbon multi-ion supercapacitors in aqueous and non-aqueous electrolytes, Energy Adv. 2 (3) (2023) 385–397, https://doi.org/10.1039/D2YA00271J.
[56] T. Panja, J. Ajuria, N. Díez, D. Bhattacharjya, E. Goikolea, D. Carriazo, Fabrication of high-performance dual carbon Li-ion hybrid capacitor: mass balancing approach to improve the energy-power density and cycle life, Sci. Rep. 10 (1) (2020) 10842, https://doi.org/10.1038/s41598-020-67216-x.
[57] N. Nieto, J. Porte, D. Saurel, L. Djuandhi, N. Sharma, A. Lopez-Urionabarrenechea, V. Palomares, T. Rojo, Use of hydrothermal carbonization to improve the performance of biowaste-derived hard carbons in sodium ion-batteries, ChemSusChem 16 (23) (2023) e202301053, https://doi.org/10.1002/cssc.202301053.
[58] K. Kim, D.G. Lim, C.W. Han, S. Osswald, V. Ortalan, J.P. Youngblood, V.G. Pol, Tailored carbon anodes derived from biomass for sodium-ion storage, ACS Sustain. Chem. Eng. 5 (10) (2017) 8720–8728, https://doi.org/10.1021/acssuschemeng.7b01497.
[59] F. Tuinstra, J.L. Koenig, Characterization of graphite fiber surfaces with Raman spectroscopy, J. Compos. Mater. 4 (4) (1970) 492–499, https://doi.org/10.1177/002199837000400405.
[60] G.G. Eshetu, T. Diemant, M. Hekmatfar, S. Grugeon, R.J. Behm, S. Laruelle, M. Armand, S. Passerini, Impact of the electrolyte salt anion on the solid electrolyte interphase formation in sodium ion batteries, Nano Energy 55 (2019) 327–340, https://doi.org/10.1016/j.nanoen.2018.10.040.
[61] Y. Pan, Y. Zhang, B.S. Parimalam, C.C. Nguyen, G. Wang, B.L. Lucht, Investigation of the solid electrolyte interphase on hard carbon electrode for sodium ion batteries, J. Electroanal. Chem. 799 (2017) 181–186, https://doi.org/10.1016/j.jelechem.2017.06.002.
[62] H. Alptekin, H. Au, E. Olsson, J. Cottom, A.C. Jensen, T.F. Headen, Q. Cai, A. J. Drew, M. Crespo Ribadeneyra, M. Titirici, Elucidation of the solid electrolyte interphase formation mechanism in micro-mesoporous hard-carbon anodes, Adv. Mater. Interfaces 9 (8) (2022) 2101267, https://doi.org/10.1002/admi.202101267.
[63] Sci-Hub | Exploring Anomalous Charge Storage in Anode Materials for Next-Generation Li Rechargeable Batteries. Chemical Reviews | https://doi.org/10.1021/acs.chemrev.9b00618. (accessed 2023-11-16).
[64] G.G. Eshetu, T. Diemant, S. Grugeon, R.J. Behm, S. Laruelle, M. Armand, S. Passerini, In-depth interfacial chemistry and reactivity focused investigation of lithium–imide- and lithium–imidazole-based electrolytes, ACS Appl. Mater. Interfaces 8 (25) (2016) 16087–16100, https://doi.org/10.1021/acsami.6b04406.
[65] M.Á. Muñoz-Márquez, M. Zarrabeitia, S. Passerini, T. Rojo, Structure, composition, transport properties, and electrochemical performance of the electrode-electrolyte interphase in non-aqueous Na-ion batteries, Adv. Mater. Interfaces 9 (8) (2022) 2101773, https://doi.org/10.1002/admi.202101773.
[66] J.F. Moulder, Handbook of X-Ray Photoelectron Spectroscopy: A Reference Book of Standard Spectra for Identification and Interpretation of XPS Data, Perkin-Elmer Corporation, 1992.
[67] X. Liu, X. Zheng, Y. Dai, W. Wu, Y. Huang, H. Fu, Y. Huang, W. Luo, Fluoride-rich solid-electrolyte-Interface enabling stable sodium metal batteries in high-safe electrolytes, Adv. Funct. Mater. 31 (30) (2021) 2103522, https://doi.org/10.1002/adfm.202103522.
[68] R. Satish, V. Aravindan, W.C. Ling, S. Madhavi, Carbon-coated Li 3 V 2 (PO 4) 3 as insertion type electrode for lithium-ion hybrid electrochemical capacitors: an evaluation of anode and cathodic performance, J. Power Sources 281 (2015) 310–317, https://doi.org/10.1016/j.jpowsour.2015.01.190.
[69] K. Karthikeyan, S. Amaresh, K.J. Kim, S.H. Kim, K.Y. Chung, B.W. Cho, Y.S. Lee, A high performance hybrid capacitor with Li2CoPO4F cathode and activated carbon anode, Nanoscale 5 (13) (2013) 5958, https://doi.org/10.1039/c3nr00760j.
[70] S.Y. Lee, J.-Y. Park, H.-J. Kim, Y.-S. Lee, Y.I. Park, Prussian blue-graphene oxide composite cathode for a sodium-ion capacitor with improved cyclic stability and energy density, J. Alloys Compd. 898 (2022) 162952, https://doi.org/10.1016/j.jallcom.2021.162952.
[71] P. Laxman Mani Kanta, M. Venkatesh, S.K. Yadav, B. Das, R. Gopalan, High energy-power characteristics of microstructurally engineered sodium vanadium phosphate in full cell level, Appl. Energy 334 (2023) 120665, https://doi.org/10.1016/j.apenergy.2023.120665.